HHS Public Access

Author manuscript

Magn Reson Med. Author manuscript; available in PMC 2018 December 01.

Published in final edited form as:

Magn Reson Med. 2017 December ; 78(6): 2106–2115. doi:10.1002/mrm.26604.

In-vivo imaging of the progression of acute lung injury using hyperpolarized [1-^{13}C] pyruvate

Mehrdad Pourfathi[1,2], **Yi Xin**[1,4], **Stephen J. Kadlecek**[1], **Maurizio F. Cereda**[3], **Harrilla Profka**[1], **Hooman Hamedani**[1,4], **Sarmad M. Siddiqui**[1,4], **Kai Ruppert**[1], **Nicholas A. Drachman**[1], **Jennia N. Rajaei**[5], and **Rahim R. Rizi**[1,*]

[1]Department of Radiology, University of Pennsylvania, Philadelphia, PA 19104, United States

[2]Department of Electrical and Systems Engineering, University of Pennsylvania, PA 19104, United States

[3]Department of Anesthesiology and Critical Care, University of Pennsylvania, PA 19104, United States

[4]Department of Bioengineering, University of Pennsylvania, PA 19104, United States

[5]School of Medicine, Stanford University, CA 94305, United States

Abstract

Purpose—To investigate pulmonary metabolic alterations during progression of acute lung injury.

Methods—Using hyperpolarized [1-^{13}C] pyruvate imaging, we measured pulmonary lactate and pyruvate in fifteen ventilated rats one, two and four hours after initiation of mechanical ventilation. Lung compliance was used as a marker for injury progression. Five untreated rats were used as controls; five rats (injured-1) received 1 ml/kg and another five rats (injured-2) received 2 ml/kg hydrochloric acid (pH 1.25) in the trachea at 70 minutes.

Results—The mean lactate-to-pyruvate ratio of the injured-1 cohort was 0.15±0.02 and 0.15±0.03 at baseline and one hour after the injury, and significantly increased from the baseline value three hours after the injury to 0.23±0.02 (p=0.002). The mean lactate-to-pyruvate ratio of the injured-2 cohort decreased from 0.14±0.03 at baseline to 0.08±0.02 one hour after the injury and further decreased to 0.07±0.02 (p=0.08) three hours after injury. No significant change was observed in the control group. Compliance in both injured groups decreased significantly after the injury (p<0.01).

Conclusion—Our findings suggest that in severe cases of lung injury, edema and hyperperfusion in the injured lung tissue may complicate interpretation of the pulmonary lactate-to-pyruvate ratio as a marker of inflammation. However, combining the lactate-to-pyruvate ratio with pulmonary compliance provides more insight into the progression of the injury and its severity.

Corresponding Author: Rahim R. Rizi, Ph.D., University of Pennsylvania, Department of Radiology, 3400 Spruce Street, MRI – Founders 1-36, Philadelphia, PA 19104, United States, Tel: 215-615-2426, rizi@uphs.upenn.edu.

Keywords

Hyperpolarization; DNP; Lungs; Pyruvate; MRI; CSI; MRSI; Carbon-13; Lung Injury; ALI; ARDS

INTRODUCTION

Acute respiratory distress syndrome (ARDS) is diagnosed in approximately 200,000 patients each year in the US, and proves fatal 40% of the time (1,2). Lung injury in ARDS is characterized by an inflammatory response that propagates in the lungs, causing capillary leakage and impaired gas exchange (2–4). ARDS is managed in the intensive care unit through careful optimization of mechanical ventilation to protect the lungs from ventilator-induced injury (2,5) as existing ventilator protocols are currently not designed to limit the spread of inflammation (2,3). Early detection of lung injury through inflammatory markers may thereby lead to improved outcomes through appropriate interventions.

Several imaging modalities such as computed tomography (CT), contrast-enhanced proton MRI and hyperpolarized MRI have been used to investigate lung injury (5–9). In our previous studies using serial CT imaging (5), we were able to visualize the spatial propagation of radiological abnormalities in the early stages of experimental injury. Other studies used hyperpolarized gas MRI to quantify alterations in the lung microstructure during mechanical ventilation (10) and lung inflammation (11,12). Although these imaging modalities elucidate the structural and functional manifestations of inflammation, they do not target the metabolic and molecular processes that drive these changes. Positron emission tomography (PET) provides visualization of metabolic changes due to lung inflammation (13–18), but this approach is limited to examining abnormalities in the uptake of the glucose analogue fluorodeoxyglucose, and is unable to reveal changes in downstream metabolism that may be crucial to the evolution of inflammation (19–21). Understanding these downstream pathways may open the road to new therapeutic approaches aimed at controlling inflammation or attenuating its consequences in the early stages (22).

Hyperpolarized carbon-13 NMR highlights changes in cellularity and metabolic pathways by quantifying downstream metabolites through their unique carbon-13 chemical shift. The temporarily enhanced carbon-13 NMR signal of hyperpolarized agents, made possible by dynamic nuclear polarization (DNP) (23), provides a sensitive molecular imaging probe to noninvasively interrogate molecular pathways and overall energy needs (24–26). Recent efforts have demonstrated the utility of this technology to probe alterations of metabolism (27–30) and pH (31) in the lungs. These studies have shown that the rate of hyperpolarized lactate labeling after injection of hyperpolarized [1-^{13}C] pyruvate in acutely inflamed lungs significantly increases. However, published work does not address the time course of early metabolic changes due to lung injury. In this study, we hypothesized that hyperpolarized [1-^{13}C] pyruvate imaging can be used to monitor progressive changes in downstream pyruvate metabolism due to progression of experimental lung injury induced by acid-aspiration.

METHODS

Animal preparation and injury protocol

A total of seventeen male Sprague Dawley rats (335±45 g) were used for this study (5 healthy, 12 injured). All animal procedures were approved by the Institutional Animal Care and Use Committee (IUCAC) of the University of Pennsylvania (Philadelphia, PA). General anesthesia was induced (40–60 mg/kg) and maintained (20 mg/kg) through intra-peritoneal administration of sodium pentobarbital every 60 minutes. The trachea was intubated with a 2-inch long, 14 gauge angiocatheter (BD, Franklin Lakes, NJ) with a sealant (UHU Tac adhesive putty; Saunders Mfg. Co. Readfield, ME) placed around the glottis to prevent gas from leaking out of the lungs. Rats were then connected to either a custom-built MR-compatible small animal ventilator or a VentElite small animal ventilator (Harvard Apparatus) and were ventilated with 100% oxygen in supine position. Animals were placed in the magnet within 10 minutes of the beginning of ventilation (t=10 min). Ventilation parameters were 8.1±0.6 ml/kg tidal volume and 8±2 cmH_2O positive end expiratory pressure (PEEP) to prevent atelectasis (alveolar collapse) and minimize ventilator-induced injury (32). Animals remained on this ventilator setting for the remainder of the study (3–4 hours) except during imaging acquisition and shimming for which PEEP was briefly reduced to 0 cmH_2O to improve field homogeneity. Peak inspiratory pressure (PIP) was monitored using an MR-compatible pressure sensor (Samba Sensors). The body temperature was monitored using a rectal thermometer and adjusted using warm air. The blood oxygen saturation level was monitored using a pulse oximeter during the scan to ensure sufficient oxygenation (S_PO_2 > 90%).

Injury was induced in twelve animals by intratracheal instillation of pH 1.25 hydrochloric acid (HCl) 70 minutes after the beginning of ventilation similar to the injury protocol used in (5); Five animals (injured-1) received 1ml/kg HCl and another seven animals (injured-2) received 2ml/kg HCl to induce more severe injury. After instillation of the acid, mechanical ventilation was resumed.

Pulmonary Compliance Measurement

Dynamic pulmonary compliance before each injection was calculated as the ratio of PIP to tidal volume in the absence of positive end-expiratory pressure and was used as a marker for lung injury (1,5)

Hyperpolarization

Pyruvate samples were prepared by mixing 14 M [1-^{13}C] pyruvate (Cambridge Isotopes), 15 mM OX063 radical (GE Healthcare) and 1.5 mM of Dotarem (Guerbet LLC). 22 μL aliquots were polarized using a commercial HyperSense DNP polarizer (Oxford Instruments) for approximately one hour. Samples were melted with 4 mL dissolution buffer (80 mM NaOH, 40 mM Trizma buffer, 50 mM NaCl and 0.1 mg/L EDTA) at 10 bar pressure and 180 ºC to yield 80 mM isotonic neutral polarized [1-^{13}C] pyruvate at 37 ºC. Polarization was estimated to be 20±6% for the studies based on the solid-state build up curve and separate measurements. Samples were transferred to the animal within approximately 10 seconds of dissolution and 6.7±1.9 ml/kg were administered through the tail vein over 10±2 seconds.

This was followed by a 300-μL saline dose over 2 seconds to flush the pyruvate from the catheter's dead volume. To minimize respiratory motion during data acquisition, a 10-second breath-hold was applied using the ventilator and data acquisition was initiated 12±1 seconds after the end of injection.

MRI/MR Spectroscopic Imaging (MRSI)

All animals were imaged using a dual-tuned $^{1}H/^{13}C$ quadrature transmit/receive birdcage coil (m2m) in a 4.7T horizontal-bore magnet (Varian Inc.) equipped with a direct drive console. Axial and coronal T_1-weighted proton images were acquired as anatomical references and to monitor the progression of the injury using a multi-slice gradient echo sequence. Imaging parameters were TR/TE=80/1.5 ms, α=20°, 128×128 matrix size, 60×60 mm^2 in-plane field of view (FOV), 100 kHz bandwidth and 16 averages. A total of 16 slices, 2 mm thick each, were acquired to cover the lungs. Manual shimming was carried out at the end of expiration using a slice-selective pulse-and-acquire sequence over a 15-mm axial slice covering the lungs.

A summary of the hyperpolarized carbon-13 imaging studies is shown in Figure 1. Fifteen animals were used for this study (5 healthy, 5 injured-1 and 5 injured-2). Each animal received three injections of hyperpolarized pyruvate at 60±6, 133±4 and 230±11 minutes after the start of ventilation except for one injured rat (injured-2) that did not survive until the third injection. Both injured cohorts (injured-1 and injured-2) received intratracheal HCl 70 minutes after starting ventilation as described earlier. Chemical shift imaging (CSI) was performed using a 2D slice selective phase-encoded free-induction decay chemical shift imaging (FID-CSI) imaging pulse sequence. Imaging parameters were TR=35 ms, 32 ms sampling time, α=12° excitation with a 200-μs Gaussian RF pulse, 16×16 matrix size, 128 spectral points, 4 kHz spectral bandwidth, 45×45 mm^2 in-plane FOV and 15 mm slice thickness with a total acquisition time of 9 seconds. This yielded a nominal in-plane spatial resolution of 2.8×2.8 mm^2. The remaining transverse magnetization at the end of each acquisition was de-phased using a 2.5-ms crusher gradient (6.5 G/cm). A 5-mm NMR tube containing 15 M solution of labeled ^{13}C urea and 5 mM gadolinium (Gd) (Omniscan, GE Healthcare) was placed in the coil next to the rat for flip angle calibration of the carbon-13 channel. A custom-designed outward spiral k-space trajectory was used in which the center of k-space was remeasured every eleventh excitation (33).

MRI Data processing

All data were processed using custom routines programmed in MATLAB 2014a (MathWorks, Inc.). A 30 Hz exponential line broadening was applied to the individual FIDs. The spatially resolved spectra were computed by applying a 3D Fourier transform to the broadened data. The periodic acquisition of the k-space center ($k_{x,y}$=0) as described in the previous section allowed pyruvate and its metabolites' time-dependences to be observed independently. These time-dependences then were used to compensate for the signal loss due to T_1 decay and other factors through amplitude normalization. This mitigated the associated blurring artifact to improve localization of the spectra. Global first order and local zero order phase corrections were applied to the real part of the spectra in each voxel followed by a 4^{th} order polynomial baseline correction. For each spectrum, the pyruvate

peak was fit to a Lorentzian function. The linewidth and the chemical shift estimates were used to fit individual Lorentzian functions to the metabolite peaks (lactate, pyruvate hydrate, bicarbonate and alanine). Metabolite maps were generated by integrating the area under the peak of the corresponding fit Lorentzian. Processed metabolite maps were converted to DICOM format and overlaid on their corresponding proton images using OsiriX 7.1 (Pixmeo SARL, Switzerland). On average, 12 voxels covering the lungs were manually selected from the MRSI/proton overlays and average pyruvate and lactate values for the lung were calculated. Average pulmonary lactate-to-pyruvate ratios were obtained by dividing the average lactate and pyruvate signals obtained from the selected voxels. We omitted quantification of alanine and bicarbonate metabolites in the lungs since their intensities are too low for accurate quantification.

Statistical Analysis

Average pulmonary pyruvate and lactate signals, lactate-to-pyruvate ratios and pulmonary compliances were exported to R (R Development Core Team, 2005) for statistical analysis. Mean values and standard errors of the pulmonary metabolite ratios and pulmonary compliance at each time point were computed for each of the three study cohorts. Two-way repeated ANOVA was used to test statistical significance between pulmonary compliance and the average pulmonary lactate-to-pyruvate ratio among different cohorts and injection times. Two-sample paired, two-tailed student's t-tests were used for *post hoc* analysis for each cohort to identify statistical significance between different injections. Two-sample unequal variance, two-tailed student's t-tests were used for each injection to assess statistical significance between the cohorts.

RESULTS

Hyperpolarized carbon-13 studies

Figures 2A–C show representative spectroscopic images overlaid on the corresponding proton images in healthy, injured-1 and injured-2 lungs. After lung injury, edematous regions are clearly visible in the posterior regions of the lungs in both injured-1 and injured-2 rats (Figs. 2B and 2C). Figures 2D–I show the close-up view of the average of the spectra in the posterior and anterior voxels in the lungs outlined in 2A–C for the healthy, injured-1 and injured-2 lungs. The average pyruvate linewidth in the healthy, injured-1 and injured-2 lungs were estimated (by the fit described in the methods section) to be 126±31Hz (2.5±0.6ppm), 97±41Hz (1.9±0.8ppm) and 57±12Hz (1.2±0.2ppm), respectively. Additionally, the pyruvate signal in both visibly edematous and non-edematous regions of the injured-2 lung increased relative to the signal in the heart after injury, as can be seen in Figs. 2H–I. While the pyruvate signal seemed to increase only in the posterior region of the injured-1 lung, as seen in figure Fig. 2F, the lactate signal increased in both anterior and posterior regions (Figs. 2F–G). The pyruvate and lactate signal are visually similar between anterior and posterior regions of the control lung (Figs. 2 D–E). The signal-to-noise ratio (SNR) of the pyruvate and lactate peaks in the spectrum obtained by averaging over the lungs was 245±70 and 58±16 for the healthy animals and 340±190 and 99±45 for the injured rats respectively. Similarly, the SNR of pyruvate and lactate peaks in the individual voxels was 93±24 and 21±5 for the healthy and 117±63 and 31±12 for the injured rats.

Figure 3 shows representative pyruvate and lactate maps at 60 and 240 minutes after the start of ventilation in rats from the control (left panel), injured-1 (middle panel) and injured-2 (right panel) cohorts. The pyruvate and lactate maps are superimposed on the corresponding proton images and are scaled to their own maximum intensity (the color map represents the intensity as fraction of the maximum value in that image). The lactate and pyruvate maps show the outline of the heart and the major vasculature in the lungs. In the control rat, there is no significant change in the pyruvate and lactate maps at these time points, indicating no detectable alteration in the lung metabolism or perfusion. In the injured-1 animal, the middle panel shows significant increase in both lactate and pyruvate signals. The left panel shows a similar pattern for the injured-2 rat; however, the pyruvate signal in the lungs increased much more significantly relative to the heart.

Figure 4A shows the average pulmonary lactate-to-pyruvate ratio for the three cohorts measured for each injection time point. There was a statistically significant difference between the lactate-to-pyruvate ratios of the three groups ($F_{2,36}$=17.34, p<0.005). Further *post hoc* analysis revealed that there was no significant difference between metabolite ratios of the cohorts before the instillation of HCl as illustrated in Fig. 4A. There was no observed difference between the lactate-to-pyruvate ratio of the injured-1 and control cohorts at the second injection (p=0.4). The lactate-to-pyruvate ratio of the injured-2 cohort was 48% lower than the control group at this time point, although this difference did not reach the level of statistical significance (p=0.06). The average lactate-to-pyruvate ratio of the injured-1 cohort at the third injection time point was significantly higher than in the healthy (p=0.005) and injured-2 (p<0.0001) cohorts. However, at the same time point, this ratio was significantly *lower* in the injured-2 cohort than in the control group (p=0.05). Figures 4B–D depict the time evolution of the lactate-to-pyruvate ratio for each cohort (mean and individual values) at different time points. Figure 4B shows that the lactate-to-pyruvate ratio of the control cohort remains unchanged in time. The lactate-to-pyruvate ratio of the injured-1 cohort (Fig. 4C) is not significantly different from baseline at the second injection time point (~1 hour after the injury); however, it increases significantly by the third injection time point (~3 hours after the injury) relative to baseline (p=0.002). The average lactate-to-pyruvate ratio of the injured-2 (Fig. 5D) cohort continuously declines at the second (p=0.18) and third (p=0.08) injection time points relative to the cohort's baseline ratio.

Figures 5A and 5B depict the average pyruvate and lactate signal intensities for all three cohorts at different time points. The intensities reported are normalized to the last solid state NMR signal level measured by the polarizer's polarimeter to account for variability in sample composition, freezing dynamics and polarizer operation. Figure 5A demonstrates that the average pyruvate signal in the injured-2 cohort is larger than in the healthy and injured-1 cohorts, although the variability of the absolute signal is large enough that this difference did not reach the level of significance ($F_{2,36=}$ 2.25, p=0.12). Figure 5B shows that the absolute lactate signal of the injured-1 rats is larger than that of the other cohorts at the third injection time-point. There was no significant difference among the cohorts' absolute lactate signals at any injection time point ($F_{2,36=}$ 2.78, p=0.18).

Pulmonary compliance

Figure 6A shows the average of the pulmonary compliances for the three cohorts before each injection. There was significant difference in compliance for the three groups ($F_{2,36}$=56.12, p<0.0001). Further *post hoc* analysis showed that there was no significant difference among the pulmonary compliance of the three cohorts before the instillation of the HCl before the first injection time point at 60 minutes. The compliance of both injured cohorts before the second and third injections was significantly lower than the control group (p<0.01). There was no significant difference between the compliance of the injured cohorts before the second (p=0.76) and third (p=0.16) injection time points.

Figures 6B–D depict the time evolution of compliance for each cohort (mean and individual values) before each injection. Figures 6C and 6D illustrate that at the second injection time point pulmonary compliance had decreased significantly from the baseline value in both injured cohorts (p<0.005) and had decreased even further by the time of the third injection (p<0.05).

The lactate-to-pyruvate ratios vs. pulmonary compliance for each animal in all three cohorts and three injection time points are plotted in Figs. 7A–C. The inner ellipses represent the 95% confidence interval of each cohort and show no segregation among the cohorts after the first injection. The second and third injections, on the other hand, show partial and complete delineation of all three cohorts, respectively.

DISCUSSION

We report enhanced lactate and pyruvate signal in the lungs after lung injury. In lungs instilled with 1ml/kg HCl we observed a significant increase in the lactate-to-pyruvate ratio 3 hours after the injury. In contrast, in lungs instilled with 2ml/kg HCl, we found a progressive decrease in the lactate-to-pyruvate ratio starting at one hour after the injury. The latter observation is likely due to greatly increased pyruvate levels in the hyperperfused lungs as seen in Figs. 2–3. This supposition is supported by earlier findings that showed an increased lung permeability index (34) and an increased pulmonary blood flow using PET (35). Despite significant variability among the cohorts' lactate-to-pyruvate ratio trends during injury progression, a combination of the lactate-to-pyruvate ratio with lung compliance provides a reliable means to separate the cohorts at the third injection time point.

The decline in pulmonary compliance after injury (Fig. 6) is a clinically relevant indicator of lung injury (1). Accumulation of excess fluid in the extracellular matrix and thickening of the alveolar walls associated with edema and inflammation give rise to this change in the mechanical characteristics of the lungs (36). The significant decrease in the lung compliance within the first hour (figure 6) is due to the reduced airspace volume arising from both the initial acid delivery and the subsequent collection of fluid in the lungs at the onset of acute injury (34). Although no significant difference was observed between the lung compliance in the injured-1 and injured-2 cohorts within the first hour, the exacerbation of the injury in both injured groups is evidenced by the significant decline of the pulmonary compliance between the second and third injection time points as shown in Figs. 6C and 6D and is suggestive of further thickening of the alveolar walls and progression of inflammation (34).

This observation is also consistent with the hyperpolarized xenon-129 studies showing thickening of the alveolar walls in the presence of inflammation (11,12).

The elevation of the lactate signal after injury is visible in Fig. 5, and is likely due to infiltration of metabolically active neutrophils in the lungs, which in early stages is known to be a consequence of an innate inflammatory response (27,37), although some of the increase could also be attributed to local hypoxia in edematous regions. The observed lactate elevation had a prominent dependent (dorsal) distribution, which can be explained by multiple factors. First, the model included HCl injection in the supine position, which likely favored a dorsal distribution of the early lesions as shown in our published studies (5). Second, dorsal hyperperfusion is characteristic of acute lung injury (38) and is likely to preferentially increase neutrophil density and extravasation in these areas of the lungs (39). It is likely that a higher tissue density, due to atelectasis and edema accumulation, increased both lactate and pyruvate signal in the dorsal regions, as images were not normalized for proton density. Lastly, incomplete recruitment of atelectatic regions during mechanical ventilation worsens injury despite the use of relatively high PEEP and low tidal volume to minimize both atelectasis and ventilator-induced stress (39,40). This is evident in the significant decline of the injured cohorts' compliance between the second and third injection time points.

Absolute concentration quantification of the metabolites (lactate, pyruvate, etc.) from the intensity of their corresponding signals is not trivial due to the variability in polarization levels and experimental setup. This is demonstrated in Fig. 6, which exhibits a large variability in the absolute signal level of the pyruvate and lactate species. To reduce this sensitivity to experimental and physiological conditions, the lactate-to-pyruvate ratio can be used instead to highlight increased glycolytic activity (24). Increased glycolysis is expected and has been previously demonstrated under conditions of anaerobic metabolism and inflammatory cell recruitment found in acute injury (13,21,28,39,41). As such, the significant increase in the lactate-to-pyruvate ratio observed at the third injection time point in the injured-1 cohort (Fig. 5A) is a surrogate for increased glycolytic activity. On the other hand, the decreased lactate-to-pyruvate ratio observed in the lungs after injury in the injured-2 rats is at odds with the observed regional lactate elevation. To explain this discrepancy, we postulate that locally increased pyruvate concentration, rather than decreased lactate production, was responsible for the low lactate-to-pyruvate in severely injured rats. The increased pyruvate concentration is due to the retention of hyperpolarized pyruvate in the extracellular space of edematous lungs (35),

Figure 6A depicts this time-dependent increase in the average pyruvate signal for the injured-2 cohort. Despite the increased availability of hyperpolarized pyruvate, its uptake at the super-physiological concentrations achieved with our injection protocol is limited by monocarboxylate transporter capacity (42,43), and conversion to lactate is limited by lactate dehydrogenase enzyme turnover and the rate at which the cofactor NADH can be regenerated (42). As a consequence, the presence of excess pyruvate in the lung tissue does not increase the lactate signal in proportion. Furthermore, the excessive accumulation of extracellular fluid in severe lung injury leads to regions of low cellular density in which

pyruvate may also accumulate, but metabolism is limited by large diffusion distances that limit delivery and transport of pyruvate into the cells (36,44).

The discrepancy between the time dependence of the lactate-to-pyruvate ratio in the injured cohorts complicates its interpretation as a single marker to assess the progression of pulmonary injury and development of inflammation. On the other hand, Fig. 6 illustrates that despite the difference between the amount of HCl instilled in the injured cohorts, there was no significant difference between the average pulmonary compliance of the injured cohorts; regardless of the injury, the compliance declines significantly throughout the course of injury. The difference between compliance in the injured and healthy animals, and the significant difference among the lactate-to-pyruvate ratio in the three cohorts at the third injection time point (Fig. 5A) suggest that the combination of lactate-to-pyruvate and compliance may enable us to better characterize the type and severity of the initial injury. Figure 7A shows great overlap among the 95% confidence regions of all three cohorts on the lactate-to-pyruvate vs. compliance graph at the first injection time point indicating no statistically significant difference between cohorts. However, as the injury progresses, each cohort follows a different trajectory on this graph, to the extent that there is a remarkable separation among the confidence regions of the cohorts at the third injection time point. This suggests that the lactate-to-pyruvate ratio provides information on the cellularity of the perfused lung volume, without which, there may be ambiguity that arises from changes in the pulmonary physiology and perfusion throughout the progression of injury.

In general, metabolic imaging of the lungs is challenging due to severe B_0 inhomogeneity, low tissue density and the lung's modest overall energy needs, which limits both the SNR and the suitability of rapid pulse sequences that are useful for imaging other organs. Despite these limitations, we were able to generate pyruvate and lactate maps with high SNR and quantify average metabolic changes in the pulmonary tissue in the presence of acute lung injury. While Fig. 2 suggests that the FID-CSI pulse sequence is capable of visualizing heterogeneity of metabolism across the lungs with sufficiently high SNR and modest spatial resolution, its utility to accurately quantify regional lactate-to-pyruvate ratio may be limited. This is primarily due to the sequence's long scan time and its susceptibility to artifacts caused by the cardiac motion and blood flow. These challenges may be partially addressed in the future by the addition of flow suppression gradients (45). Alternatively, rapid high resolution pulse sequences, specific to lung spectroscopic imaging, can be developed for the future studies to circumvent these limitations (46).

The lungs receive the full blood supply during each circulation and perform a variety of biochemical functions to maintain body homeostasis. These functions can change substantially and detrimentally in patients suffering from ARDS or other conditions such as pulmonary fibrosis or sepsis, which result in lactic acid release from the lungs (22,47). Such changes are part of a spectrum of multi-organ dysfunctions and are associated with a high mortality (2,48,49). Consequently, the development of molecular imaging techniques that facilitate direct interrogation of the lung metabolism, and its spatial heterogeneity, can provide more insight into the relationship between abnormalities in mechanics and cellularity of diseased lung tissue. Addressing this knowledge gap is relevant to clinical efforts to improve evaluation of inflammatory lung disorders and can potentially result in

more effective and specific early intervention. This setting presents unique challenges and opportunities to characterize metabolic flux in acute lung injury models using hyperpolarized carbon-13 technology.

CONCLUSION

In this study, we used hyperpolarized [1-^{13}C] pyruvate to investigate metabolic changes in the lung parenchyma during the development and progression of acute lung injury. We demonstrated increased pyruvate signal, likely due to increased capillary permeability, and increased lactate signal due to neutrophilic infiltration after the injury. This is consistent with previous studies that investigated early changes in blood flow in the lung's immunological response to acid aspiration-induced ARDS (34,35). The lactate-to-pyruvate ratio in lungs injured with instillation of 1 ml/kg HCl increased within three hours of injury. However, this ratio decreased in lungs instilled with 2 ml/kg of HCl. The latter observation was likely a result of increased pyruvate availability due to locally increased blood flow, water volume and vascular permeability. Our findings suggest that the lactate-to-pyruvate ratio can be used as a marker of progression of lung inflammation in certain cases, although regional changes to the lung blood flow may complicate its use as a single marker of inflammation-related lactate production. However, combining the lactate-to-pyruvate ratio with pulmonary compliance not only can differentiate between the healthy and injured animals, but it provides more insight into the severity of the inflammation and edema three hours after the injury.

Acknowledgments

We would like to thank Dr. Stephen Pickup for his assistance with the MRI pulse sequences. This work was supported by the National of Institutes of Health (NIH) R01 HL124986.

References

1. Acute Respiratory Distress Syndrome: The Berlin Definition. JAMA. 2012; 307:2526–2533. DOI: 10.1001/jama.2012.5669 [PubMed: 22797452]
2. Johnson ER, Matthay MA. Acute Lung Injury: Epidemiology, Pathogenesis, and Treatment. Journal of Aerosol Medicine and Pulmonary Drug Delivery. 2010; 23:243–252. DOI: 10.1089/jamp.2009.0775 [PubMed: 20073554]
3. Fanelli V, Ranieri VM. Mechanisms and Clinical Consequences of Acute Lung Injury. Annals ATS. 2015; 12:S3–S8. DOI: 10.1513/AnnalsATS.201407-340MG
4. Tabuchi A, Nickles HT, Kim M, Semple JW, Koch E, Brochard L, Slutsky AS, Pries AR, Kuebler WM. Acute Lung Injury Causes Asynchronous Alveolar Ventilation That Can Be Corrected by Individual Sighs. Am J Respir Crit Care Med. 2016; 193:396–406. DOI: 10.1164/rccm.201505-0901OC [PubMed: 26513710]
5. Cereda M, Xin Y, Meeder N, et al. Visualizing the Propagation of Acute Lung Injury. Anesthesiology [Internet]. 2016; 124:121–131. DOI: 10.1097/ALN.0000000000000916
6. Mistry NN, Pollaro J, Song J, De Lin M, Johnson GA. Pulmonary perfusion imaging in the rodent lung using dynamic contrast-enhanced MRI. Magn Reson Med [Internet]. 2008; 59:289–297. DOI: 10.1002/mrm.21353
7. Bomanji J, Almuhaideb A, Zumla A. Combined PET and X-ray computed tomography imaging in pulmonary infections and inflammation. Current Opinion in Pulmonary Medicine. 2011; 17:197–205. DOI: 10.1097/MCP.0b013e328344db8a [PubMed: 21358408]

8. Mills GH. Functional magnetic resonance imaging of the lung. British Journal of Anaesthesia. 2003; 91:16–30. DOI: 10.1093/bja/aeg149 [PubMed: 12821562]

9. Hamedani H, Kadlecek SJ, Ishii M, et al. Alterations of Regional Alveolar Oxygen Tension in Asymptomatic Current Smokers: Assessment with Hyperpolarized 3He MR Imaging. Radiology. 2015; 274:585–596. DOI: 10.1148/radiol.14132809 [PubMed: 25322340]

10. Cereda, M., Emami, K., Kadlecek, S., et al. Quantitative imaging of alveolar recruitment with hyperpolarized gas MRI during mechanical ventilation. jap.physiology.org

11. Ouriadov A, Fox M, Hegarty E, Parraga G, Wong E, Santyr GE. Early stage radiation-induced lung injury detected using hyperpolarized 129Xe Morphometry: Proof-of-concept demonstration in a rat model. Magn Reson Med. 2015; n/a–n/a. doi: 10.1002/mrm.25825

12. Li H, Zhang Z, Zhao X, Sun X, Ye C, Zhou X. Quantitative evaluation of radiation-induced lung injury with hyperpolarized xenon magnetic resonance. Magn Reson Med. 2015; n/a–n/a. doi: 10.1002/mrm.25894

13. Bellani G, Messa C, Guerra L, Spagnolli E, Foti G, Patroniti N, Fumagalli R, Musch G, Fazio F, Pesenti A. Lungs of patients with acute respiratory distress syndrome show diffuse inflammation in normally aerated regions: A [18F]-fluoro-2-deoxy-D-glucose PET/CT study. Critical Care Medicine. 2009; 37:2216–2222. DOI: 10.1097/CCM.0b013e3181aab31f [PubMed: 19487931]

14. Chen DL, Rosenbluth DB, Mintun MA, Schuster DP. FDG-PET imaging of pulmonary inflammation in healthy volunteers after airway instillation of endotoxin. J Appl Physiol. 2006; 100:1602–1609. DOI: 10.1152/japplphysiol.01429.2005 [PubMed: 16424067]

15. de Prost N, Tucci MR, Melo MFV. Assessment of Lung Inflammation With 18F-FDG PET During Acute Lung Injury. American Journal of Roentgenology. 2010; 195:292–300. DOI: 10.2214/AJR.10.4499 [PubMed: 20651183]

16. Chen DL, Ferkol TW, Mintun MA, Pittman JE, Rosenbluth DB, Schuster DP. Quantifying Pulmonary Inflammation in Cystic Fibrosis with Positron Emission Tomography. Am J Respir Crit Care Med. 2006; 173:1363–1369. DOI: 10.1164/rccm.200506-934OC [PubMed: 16543553]

17. Neeb D, Kunz RP, Ley S, Szábo G, Strauss LG, Kauczor H-U, Kreitner K-F, Schreiber LM. Quantification of pulmonary blood flow (PBF): Validation of perfusion MRI and nonlinear contrast agent (CA) dose correction with H 215O positron emission tomography (PET). Magn Reson Med. 2009; 62:476–487. DOI: 10.1002/mrm.22025 [PubMed: 19488992]

18. Locke LW, Williams MB, Fairchild KD, et al. FDG-PET Quantification of Lung Inflammation with Image-Derived Blood Input Function in Mice. International Journal of Molecular Imaging. 2011; 2011:1–6. DOI: 10.1155/2011/356730

19. Xie N, Tan Z, Banerjee S, Cui H, Ge J, Liu R-M, Bernard K, Thannickal VJ, Liu G. Glycolytic Reprogramming in Myofibroblast Differentiation and Lung Fibrosis. Am J Respir Crit Care Med. 2015; 192:1462–1474. [PubMed: 26284610]

20. Tierney, DF., Young, SL. Glucose and Intermediary Metabolism of the Lungs. Hoboken, NJ, USA: John Wiley & Sons, Inc; 2011.

21. Cohen GM. Pulmonary metabolism of foreign compounds: its role in metabolic activation. Environmental Health Perspectives. 1990; 85:31–41. [PubMed: 2200668]

22. Kottmann RM, Kulkarni AA, Smolnycki KA, et al. Lactic Acid Is Elevated in Idiopathic Pulmonary Fibrosis and Induces Myofibroblast Differentiation via pH-Dependent Activation of Transforming Growth Factor-β. Am J Respir Crit Care Med. 2012; 186:740–751. DOI: 10.1164/rccm.201201-0084OC [PubMed: 22923663]

23. Ardenkjaer-Larsen JH. Increase in signal-to-noise ratio of > 10,000 times in liquid-state NMR. Proceedings of the National Academy of Sciences. 2003; 100:10158–10163. DOI: 10.1073/pnas.1733835100

24. John Kurhanewicz Daniel B, Vigneron Brindle K, et al. Analysis of Cancer Metabolism by Imaging Hyperpolarized Nuclei: Prospects for Translation to Clinical Research. NeoPlasia. 2011; : 81–97. DOI: 10.1593/neo.101102 [PubMed: 21403835]

25. Golman K, Olsson LE, Axelsson O, Månsson S, Karlsson M, Petersson JS. Molecular imaging using hyperpolarized 13C. BJR. 2003; 76:S118–S127. DOI: 10.1259/bjr/26631666 [PubMed: 15572334]

26. Nelson SJ, Kurhanewicz J, Vigneron DB, et al. Metabolic Imaging of Patients with Prostate Cancer Using Hyperpolarized [1-13C]Pyruvate. Science Translational Medicine. 2013; 5:198ra108–198ra108. DOI: 10.1126/scitranslmed.3006070
27. Shaghaghi H, Kadlecek S, Deshpande C, Siddiqui S, Martinez D, Pourfathi M, Hamedani H, Ishii M, Profka H, Rizi R. Metabolic spectroscopy of inflammation in a bleomycin-induced lung injury model using hyperpolarized 1- 13C pyruvate. NMR Biomed. 2014; n/a–n/a. doi: 10.1002/nbm.3139
28. Pullinger B, Profka H, Ardenkjaer-Larsen JH, Kuzma NN, Kadlecek S, Rizi RR. Metabolism of hyperpolarized [1-13C]pyruvate in the isolated perfused rat lung - an ischemia study. NMR Biomed. 2012; n/a–n/a. doi: 10.1002/nbm.2777
29. Thind K, Jensen MD, Hegarty E, Chen AP, Lim H, Martinez-Santiesteban F, Van Dyk J, Wong E, Scholl TJ, Santyr GE. Mapping metabolic changes associated with early Radiation Induced Lung Injury post conformal radiotherapy using hyperpolarized 13C-pyruvate Magnetic Resonance Spectroscopic Imaging. Radiotherapy and Oncology. 2014; 110:317–322. DOI: 10.1016/j.radonc.2013.11.016 [PubMed: 24440041]
30. Shaghaghi H, Kadlecek S, Siddiqui S, pourfathi M, Hamedani H, Clapp J, Profka H, Rizi R. Ascorbic acid prolongs the viability and stability of isolated perfused lungs: A mechanistic study using (31)P and hyperpolarized (13)C nuclear magnetic resonance. Free Radical Biology and Medicine [Internet]. 2015; 89:62–71. DOI: 10.1016/j.freeradbiomed.2015.06.042
31. Drachman N, Kadlecek S, pourfathi M, Xin Y, Profka H, Rizi R. In vivo pH mapping of injured lungs using hyperpolarized [1-(13) C]pyruvate. Magn Reson Med. 2016; doi: 10.1002/mrm.26473
32. FRANK JA, GUTIERREZ JA, JONES KD, ALLEN L, DOBBS L, Matthay MA. Low Tidal Volume Reduces Epithelial and Endothelial Injury in Acid-injured Rat Lungs. Am J Respir Crit Care Med. 2002; 165:242–249. DOI: 10.1164/ajrccm.165.2.2108087 [PubMed: 11790662]
33. Kadlececk, S., Pourfathi, M., Profka, H., Rizi, RR. A Method to Identify and Correct for Blurring Artifacts in Hyperpolarized Metabolic Imaging. Abstract 3533, The 24th Annual Meeting of ISMRM; 2016;
34. KENNEDY TP, JOHNSON KJ, KUNKEL RG, WARD PA, KNIGHT PR, FINCH JS. Acute Acid Aspiration Lung Injury in the Rat - Biphasic Pathogenesis. Anesth Analg. 1989; 69:87–92. [PubMed: 2742173]
35. Richter T, Bergmann R, Knels L, Hofheinz F, Kasper M, Deile M, Pietzsch J, Ragaller M, Koch T. Pulmonary Blood Flow Increases in Damaged Regions Directly after Acid Aspiration in Rats. Anesthesiology. 2013; 119:890–900. DOI: 10.1097/ALN.0b013e3182a17e5b [PubMed: 23846582]
36. Matute-Bello G, Frevert CW, Martin TR. Animal models of acute lung injury. American Journal of Physiology - Lung Cellular and Molecular Physiology. 2008; 295:L379–L399. DOI: 10.1152/ajplung.00010.2008 [PubMed: 18621912]
37. Thind K, Chen A, Friesen-Waldner L, Ouriadov A, Scholl TJ, Fox M, Wong E, VanDyk J, Hope A, Santyr G. Detection of radiation-induced lung injury using hyperpolarized 13C magnetic resonance spectroscopy and imaging. Magn Reson Med. 2012; n/a–n/a. doi: 10.1002/mrm.24525
38. Schuster DP, Anderson C, Kozlowski J, Lange N. Regional pulmonary perfusion in patients with acute pulmonary edema. J Nucl Med. 2002; 43:863–870. DOI: 10.1056/NEJM197703032960903 [PubMed: 12097454]
39. de Prost N, Feng Y, Wellman T, et al. 18F-FDG kinetics parameters depend on the mechanism of injury in early experimental acute respiratory distress syndrome. PubMed - NCBI J Nucl Med. 2014; 55:1871–1877. DOI: 10.2967/jnumed.114.140962
40. Wellman TJ, Winkler T, Costa ELV, Musch G, Harris RS, Zheng H, Venegas JG, Vidal Melo MF. Effect of Local Tidal Lung Strain on Inflammation in Normal and Lipopolysaccharide-Exposed Sheep*. Critical Care Medicine. 2014; 42:e491–e500. DOI: 10.1097/CCM.0000000000000346 [PubMed: 24758890]
41. Daniels CJ, McLean MA, Schulte RF, et al. A comparison of quantitative methods for clinical imaging with hyperpolarized 13C-pyruvate. NMR Biomed. 2016; doi: 10.1002/nbm.3468
42. Kadlecek S, Shaghaghi H, Siddiqui S, Profka H, Pourfathi M, Rizi R. The effect of exogenous substrate concentrations on true and apparent metabolism of hyperpolarized pyruvate in the

isolated perfused lung Rizi RR, editor. NMR Biomed [Internet]. 2014; 27:1557–1570. DOI: 10.1002/nbm.3219

43. Johnson ML, Hussien R, Horning MA, Brooks GA. Transpulmonary pyruvate kinetics. AJP: Regulatory, Integrative and Comparative Physiology. 2011; 301:R769–R774. DOI: 10.1152/ajpregu.00206.2011
44. Scallan J, Huxley VH, Korthuis RJ. Pathophysiology of Edema Formation. 2010
45. Gordon JW, Niles DJ, Adamson EB, Johnson KM, Fain SB. Application of flow sensitive gradients for improved measures of metabolism using hyperpolarized 13c MRI. Magn Reson Med. 2015; n/a–n/a. doi: 10.1002/mrm.25584
46. Pourfathi, M., Kadlecek, S., Profka, H., Siddiqui, S., Gatens, H., Rizi, R. Towards High Resolution Chemical Shift Imaging of the Lungs using Hyperpolarized Carbon-13. Abstract 3533, The 24th Annual Meeting of ISMRM; 2015;
47. Kellum JA, Kramer DJ, Lee K. Release of lactate by the lung in acute lung injury. CHEST …. 1997
48. Garcia-Alvarez M, Marik P, Bellomo R. Sepsis-associated hyperlactatemia. Critical Care. 2014; 18:5.2014; 18:1.doi: 10.1186/s13054-014-0503-3
49. Adrogue HJ. Metabolic acidosis: pathophysiology, diagnosis and management. Journal of Nephrology. 2006; 19:S62–S69. [PubMed: 16736443]

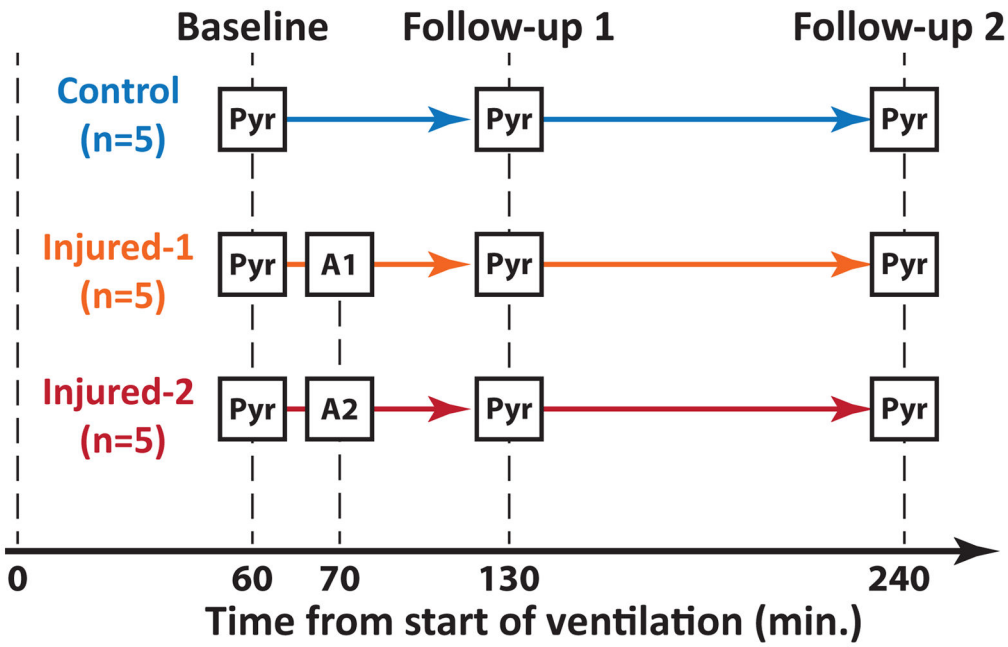

Figure 1.

Study design for the hyperpolarized pyruvate studies. Three cohorts of rats (5 each) were used. Each rat received 3 injections of hyperpolarized [1-13C] pyruvate (Pyr) at approximately 60, 130 and 240 minutes after the start of ventilation. The injured-1 cohort received 1 ml/kg HCl (A1) and the injured-2 received 2 ml/kg HCl (A2) intratracheally 10 minutes after the first pyruvate injection. Compliance was measured before each pyruvate injection.

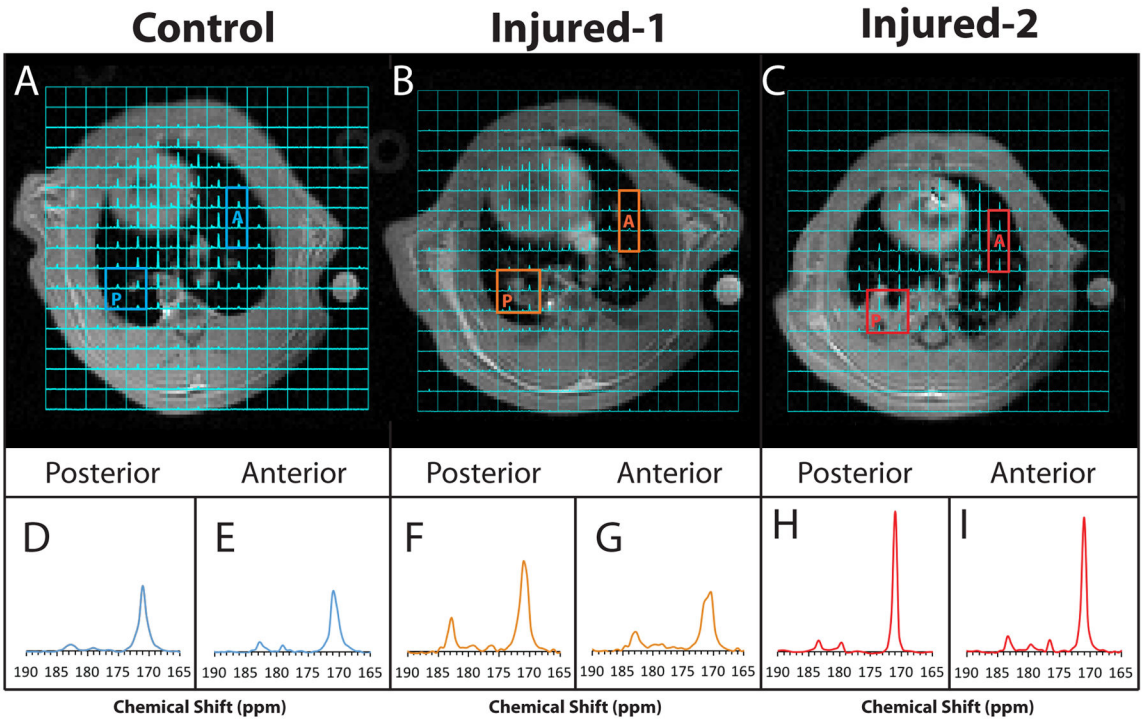

Figure 2.

Representative carbon-13 MRSI overlay on 1H images in (A) healthy and (B) injured-1 and (C) injured-2 rat. The bottom panels show the close-up view of the average of spectra in the posterior voxels (D,F,H) and anterior voxels (E,G,I) outlined in (A–C) for the healthy, injured-1 and injured-2 lungs. The pyruvate and lactate signal in both anterior and posterior voxels of the control rat seem to be similar. In the injured-1 rat, the overall pyruvate and lactate signal increased in the posterior voxels (F) and the lactate signal increased in the interior voxels (G). whereas the pyruvate signal increased significantly in the injured-2 rat in both areas (H, I). At the same time, the linewidth in the injured-2 rat became narrower, which was likely due to formation of edema and consequent improvement of local field homogeneity.

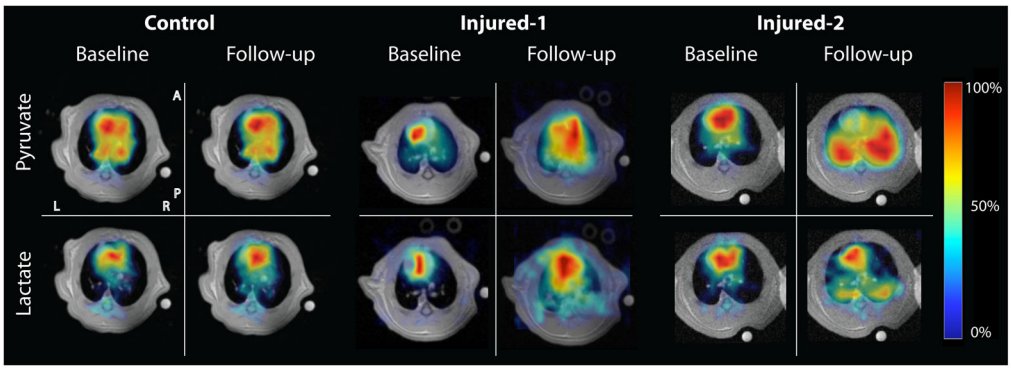

Figure 3.

Representative pyruvate and lactate maps overlaid on their corresponding proton images. The left panel shows a healthy rat (right panel) 60 (baseline) and 240 (follow-up) minutes after the start of ventilation. The middle and right panels show representative metabolite maps in injured-1 and injured-2 animals at the same time points, corresponding to before (baseline) and 240 minutes after (follow-up) the acid aspiration injury. The color bar maps the intensity of each metabolite image as a fraction of the maximum value in the same image.

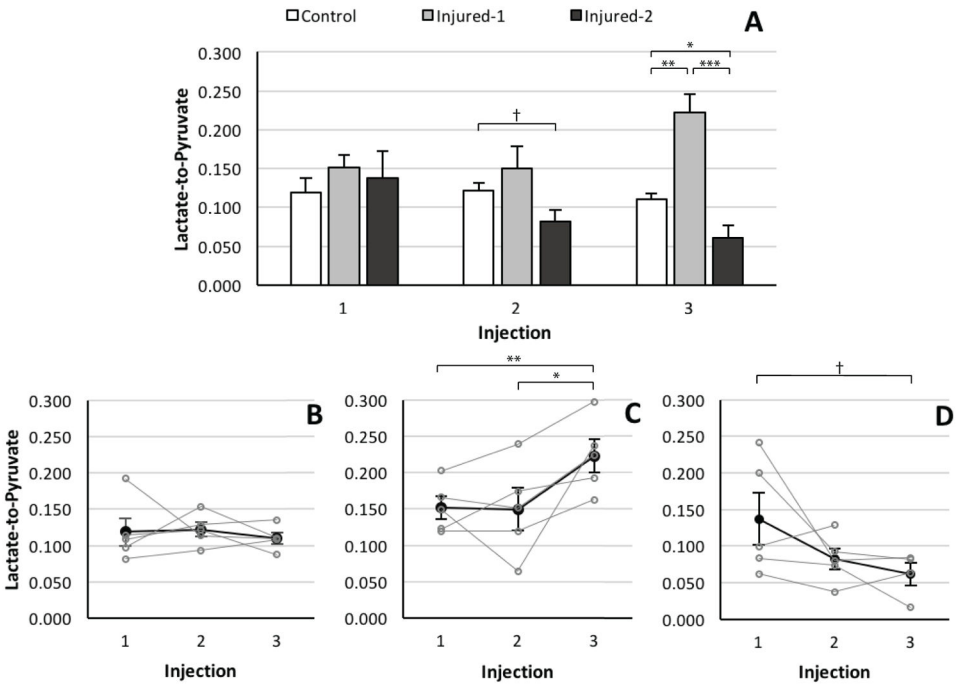

Figure 4.

(A) Average pulmonary lactate-to-pyruvate ratio in control (white), injured-1 (light gray) and injured-2 (dark gray) cohorts for all injections. Average (dark filled circles) and individual (gray hollow circles) pulmonary lactate-to-pyruvate ratios in (B) control (C) Injured-1 and (D) injured-2 cohorts for all three injections. (*** p<0.001, ** p <0.01, * p <0.05, † p <0.1)

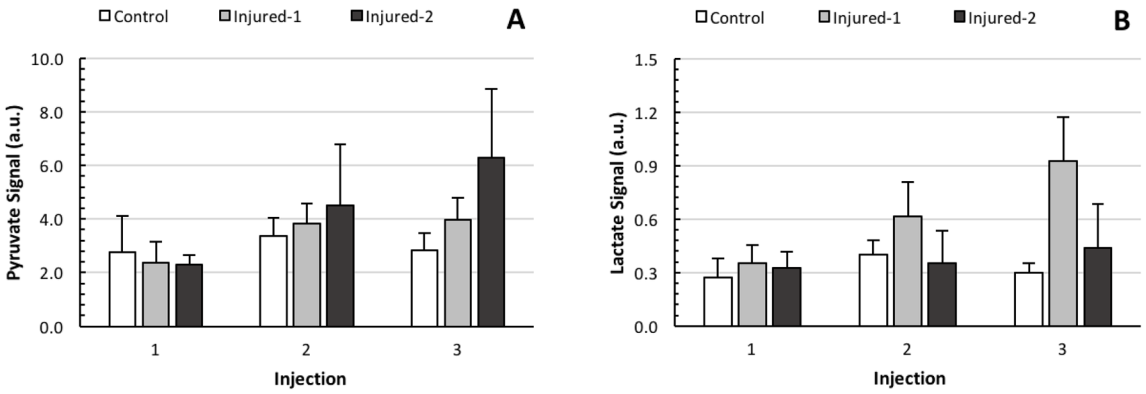

Figure 5.

Average (A) pyruvate signal and (B) lactate signal, corrected for solid-state polarization levels, for the three cohorts and for all three injections.

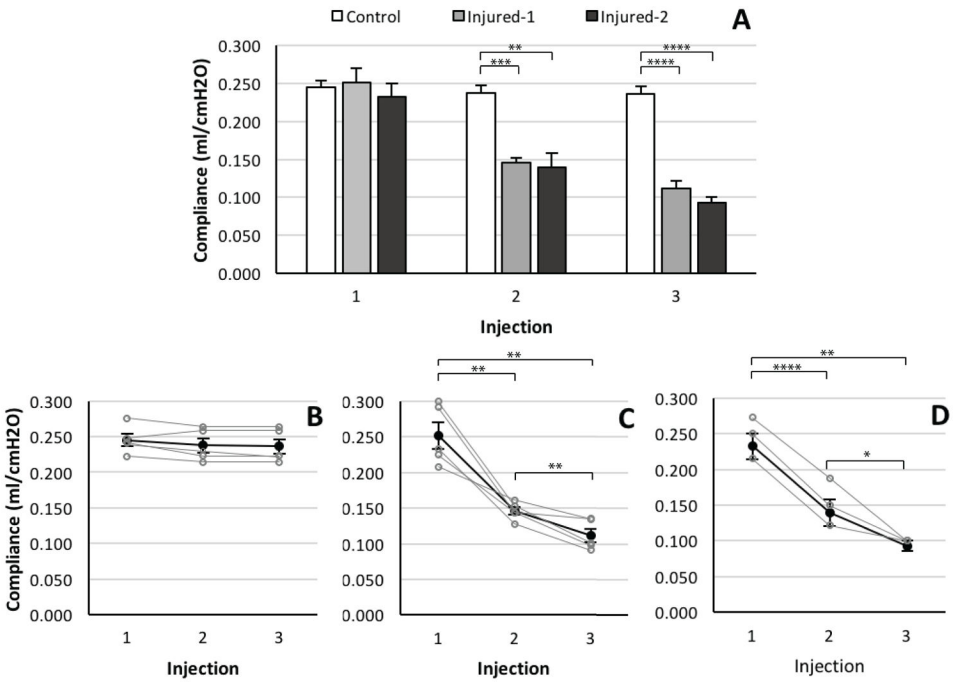

Figure 6.

(A) Average pulmonary compliance in control (white), injured-1 (light gray) and injured-2 (dark gray) cohorts for all injections. Average (dark filled circles) and individual (gray hollow circles) pulmonary compliance in (B) control (C) injured-1 and (D) injured-2 cohorts for all injections. (**** p <0.0001, *** p <0.001, ** p <0.01, * p <0.05)

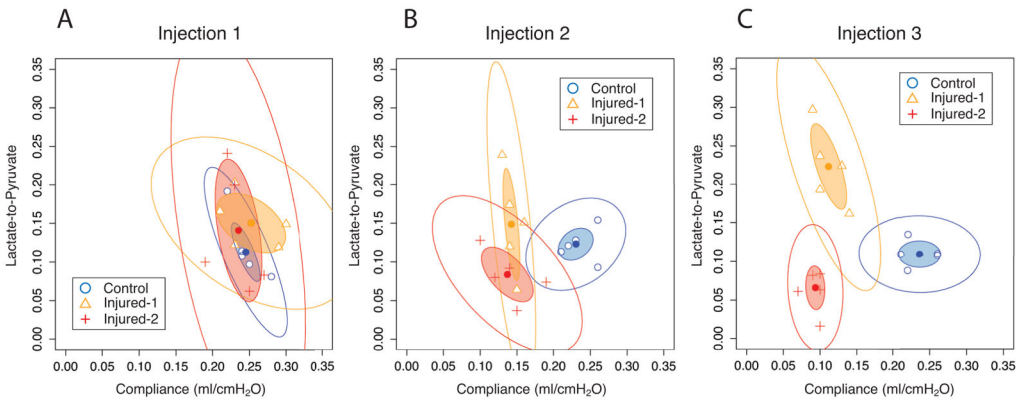

Figure 7.

Lactate-to-pyruvate vs. pulmonary compliance for the control (circles), injured-2 (triangles) and injured-2 (crosses) cohorts at first (A), second (B) and third (C) injection time points. Inner and outer ellipses represent 95% and 99% confidence intervals, respectively.